Lattice dynamics and thermal properties of phononic semiconductors

S. P. Hepplestone* and G. P. Srivastava
School of Physics, University of Exeter, Exeter EX4 4QL, United Kingdom
(Received 23 March 2011; revised manuscript received 11 August 2011; published 27 September 2011)

An enhanced adiabatic bond charge model has been employed to study the lattice dynamics of phononic metamaterials based on group-IV and group–III-V semiconductors. Using the full phonon spectrum and a realistic Brillouin zone summation method, we have developed theories of phonon scattering rates from interface formation and anharmonicity. Numerical results for specific-heat capacity and phonon conductivity of thin Si/Ge and GaAs/AlAs superlattices are then presented and compared with available experimental measurements. The roles of various phonon scattering mechanisms in controlling the thermal conductivity in different temperature ranges have been quantified.

DOI: 10.1103/PhysRevB.84.115326 PACS number(s): 63.22.Np, 43.35.+d, 68.35.Iv

I. INTRODUCTION

Nanostructured semiconductors show several fascinating properties such as exceptionally low thermal conductivity, low or negative phonon group velocity, and stop bands in the phonon spectra. Such structures are of interest as, in such systems, it is possible to engineer properties not inherent to either of the two constituent materials, rendering them very useful in future technological applications. These are often referred to as metamaterials. Phononic crystals are an important subclass of metamaterial[1] that exhibit novel thermal properties. These represent an example of acoustic metamaterials and are based upon periodic arrangement of two or more different materials with contrasting vibrational properties, and have been fabricated as solid-air[2] and solid-fluid[3] composites on the scale of μm-mm. Technological advances have led to the fabrication of nanophononic solid-solid composites.[4] Such structures exhibit ultralow thermal conductivity along growth direction when compared with either of the two bulk constituents. For Si/Ge superlattices, there is a drop in thermal conductivity of more than a factor of 100 at room temperature and below.[5] Engineering a metamaterial with a very low thermal conductivity has exciting applications for thermoelectrics.

What governs the low thermal conductivity of such materials is still being investigated. For superlattices, a considerable amount of work has been previously carried out. Experimental measurements show that the thermal conductivity is clearly dependent on the period of the superlattice, its constituent materials, and the temperature. A thorough review of these points was presented by Cahill.[5] Several theoretical papers have attempted to provide an explanation, but no consensus has been reached. In our previous paper, we have presented a further brief review of the various existing theoretical discussions.[6]

To understand the low thermal conductivity of nanophononic composite systems, we first refer to the simple kinetic model for thermal conductivity κ:

$$\kappa = \tfrac{1}{3} C_v v \Lambda, \tag{1}$$

where C_v is the phonon heat capacity, v is the average phonon velocity, and Λ is the average lifetime of the phonons in the system. To understand the thermal properties of nanopatterned acoustic metamaterials, one has to understand each of these three terms. Each of these terms can be calculated from the phonon dispersion relations in the system. For phonon dispersion relations, the traditional theory in metamaterials treats these systems as elastic media and deals with the propagation of only longitudinal acoustic (LA) modes.[4,7,8] Similarly, traditional theories of phonon lifetime and specific-heat capacity are based on the continuum theory[9–13] and fail to account for the atomic behavior or confinement effects. Most importantly, when explaining the thermal conductivity, almost all approaches only focus on one of the terms presented in Eq. (1) without considering the effect of the other factors.

In this paper, we present a comprehensive study of each of the terms presented in Eq. (1) and examine how they help explain the low thermal conductivity of semiconductor superlattices. In Sec. II, we have employed an extended adiabatic bond charge model (EBCM) to present lattice dynamical results of different types of nanostructured metamaterials, based on tetrahedrally bonded semiconductors, in the form of superlattices and embedded nanowires. We further discuss the effects of the structuring of these materials on the group velocity of the phonon modes. In Sec. III, we present, using the full phonon spectrum (i.e., including acoustic as well as optical phonons of both transverse and longitudinal polarizations) an atomic-scale theory of phonon scattering to discuss the lifetime term. In this paper, we discuss the effect the formation of acoustic metamaterials will have on phonon scattering due to interfaces and on anharmonic phonon scattering rates (including both normal and umklapp processes). In Sec. IV, we discuss the specific-heat capacity of several superlattice (SL) systems, discussing the effects of periodicity and composition of unit cells. We then present in Sec. V a comprehensive discussion of the thermal conductivity of superlattices. The theory has been applied to quantitatively explain experimentally measured results for the thermal conductivity, and its variation with period and temperature, of metamaterials in the form of Si/Ge and GaAs/AlAs superlattices.

II. LATTICE DYNAMICS

The adiabatic bond charge model (BCM), originally developed by Weber,[14] is one of the most successful and physically appealing phenomenological atomic-scale lattice dynamical theories for semiconductors. It has been applied

to tetrahedrally bonded semiconductors and their surfaces with remarkable ease.[15] The quality of BCM results has been favorably discussed for bulk,[16] surfaces,[17] and alloys.[18] We have also presented an enhanced version of this model, the EBCM or enhanced bond charge model, which has successfully been applied to nanostructured semiconductor structures.[18] In the BCM, the valence charge density is considered as point charges, called bond charges (BCs), located along the bonds between nearest-neighbor atoms. The location of a BC is chosen according to the polarity of the bond under consideration. For a semiconductor of ionicity p, a BC is located at a distance $p\%$ from the center of the bond toward the more electronegative atomic species. The BCs are assumed to have zero mass and are allowed to follow ions adiabatically. Lattice dynamical equations of motion for the ions and the BCs are set up by considering three types of interaction: (i) Coulomb interaction between all particles within the structure (ion-ion, ion-BC, BC-BC), which is evaluated using the Ewald summation technique; (ii) short-range central force interaction acting between nearest neighbors (ion-ion, ion-BC, BC-BC); and (iii) a rotationally invariant Keating-type bond bending interaction,[19] depending on the BC ion–BC angle. Such an approach requires four (six) parameters to model the phonon dispersion relations of IV-IV (III-V) bulk semiconductors. In the EBCM, the parameters for the individual systems studied here are taken from previous works.[15] Interaction parameters required for dealing with bonds at interfaces in composite structures are taken as appropriately weighted average values for the two constituent materials. While strain effects may lead to some changes in phonon frequencies, the overall effect is not expected to be significant, especially as the modeled parameters produce phonon dispersion results for Si_xGe_{1-x} alloys in good agreement with experimental measurements.[20]

We have successfully applied the EBCM to study the lattice dynamics of several different systems, including bulk semiconductors, semiconductor surfaces, nanostructures, and acoustic metamaterials.[18] In particular, for the results presented here, we note good agreement with experimental measurements for the location and size of the longitudinal acoustic and transverse acoustic (LA-TA) gaps for Si(4 nm)/$Si_{0.4}Ge_{0.6}$(8 nm)[001] (Ref. 4) and GaAs(23)/AlAs(9)[001] (Ref. 21) superlattices (see Ref. 18). A further validation of the presently adopted EBCM is established by noting very good agreement between our results and previously understood trends for the highest optical phonon mode in superlattices of various periods.[22,23]

Phonon frequencies in solids typically range between 0 and 50 THz, with acoustic modes not exceeding 30 THz or so. For considerations of phonon generation, propagation, and detection, it is useful to consider the following frequency categories: sonic range (below KHz), ultrasonic range (KHz–MHz), hypersonic range (GHz–THz), and optical range (several THz). The results will be discussed with two specific features in mind: confinement of modes and frequency gaps in dispersion curves. In particular, we will investigate *polarization gaps* and *full gaps* arising from the formation of the metamaterial structure. A polarization gap will be taken as the frequency gap in the dispersion curve for a phonon branch of a particular polarization (transverse or longitudinal) branch. A full gap will indicate a gap common to all polarizations. It will be helpful to further classify a full gap as one dimensional, two dimensional, or three dimensional when it exists along one, two, or three unrelated directions in the Brillouin zone for the metamaterial. We may also refer to a structure as *n-D phononic* if the full gap is n dimensional. It is important to note, though, that all the systems discussed here are full three-dimensional materials and are not confined systems (such as isolated nanowires or nanodots).

A. Superlattices

We will consider superlattices $A(m)/B(n)$ grown along the [001] direction with each repeat period containing m atomic layers of material A and n atomic layers of material B. Panels (a) and (b) in Fig. 1 show the phonon dispersion curves for bulk Si, bulk Ge, the Si(19)/Ge(5) superlattice, and the Si(72)/Ge(30) superlattice. Both these superlattices have been fabricated by Lee *et al.*,[24] who have quoted their periods as 33 and 140 Å, respectively. A comparison of results for the superlattices and bulk materials clearly reveals that the superlattice dispersion relations are characterized by zone-folded branches, shallow dispersive acoustic branches, flat (dispersionless) optical branches, and polarization gaps at the zone center and the zone edge. The existence of two clear gaps has been highlighted (in blue color) for the Si(72)/Ge(30) superlattice in a narrow acoustic frequency range 18–38 cm^{-1}. For a better discussion of frequency gaps, we present in Fig. 2 the phonon dispersion curves for the thin SLs Si(2)/Ge(2), Si(2)/Sn(2),

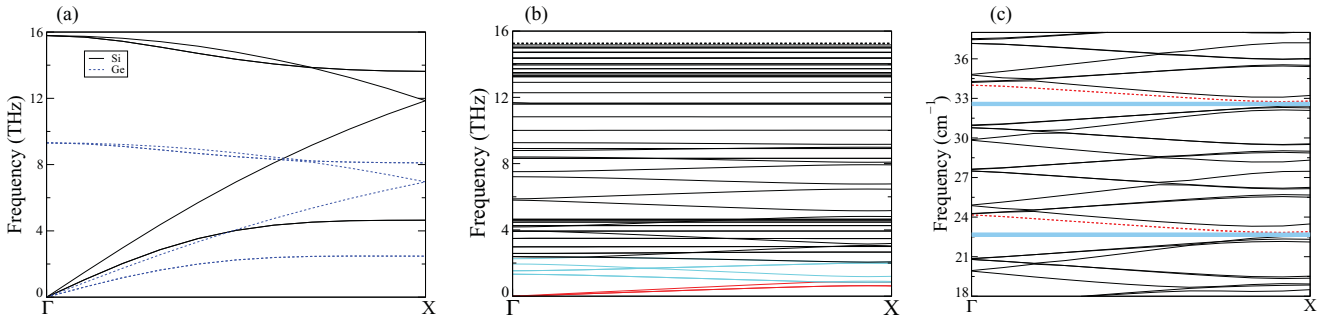

FIG. 1. (Color online) Phonon dispersion curves for (a) bulk Si and Ge semiconductors, (b) Si(19)/Ge(5)[001] superlattice, and (c) Si(72)/Ge(30)[001] superlattice. For clarity, for the superlattices we have highlighted the three acoustic branches in red and the folded acoustic branches in blue, and the highest optical branch as a black dashed line.

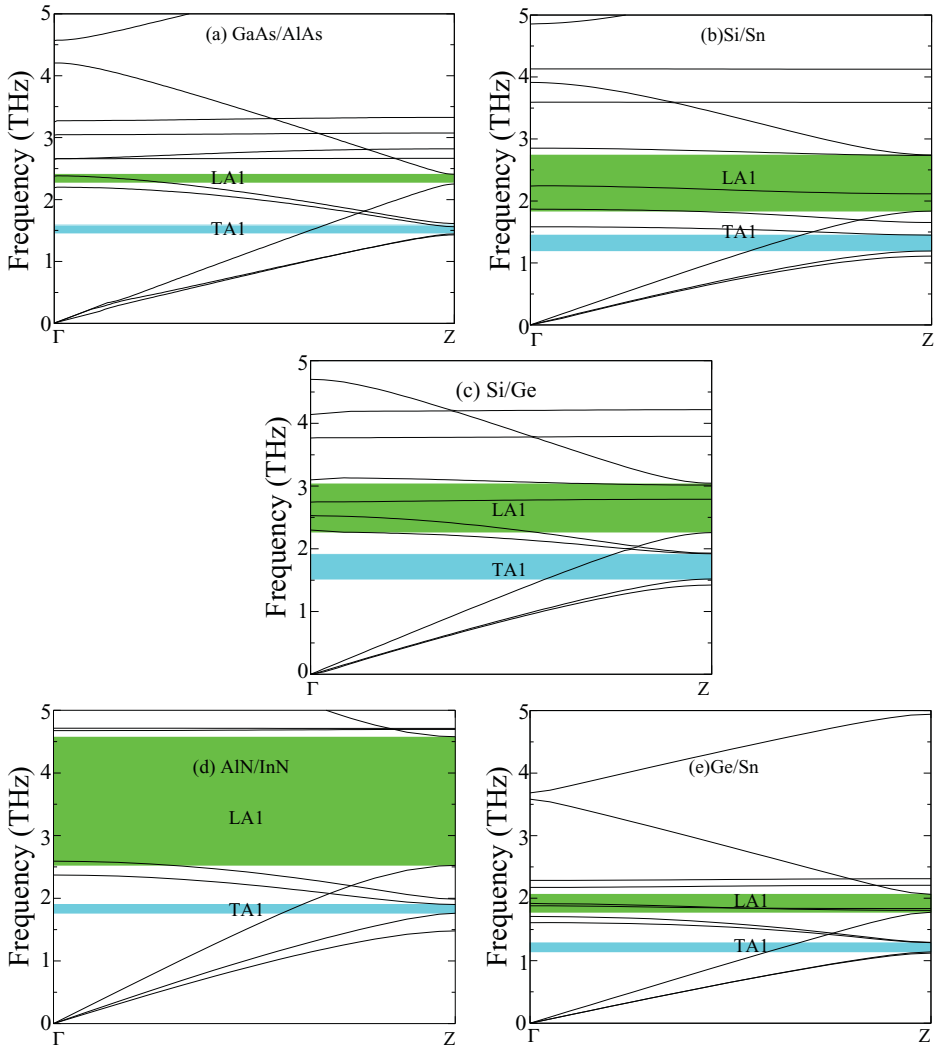

FIG. 2. (Color online) Phonon dispersion curves for the Si(2)/Sn(2), Ge(2)/Sn(2), GaAs(2)/AlAs(2), and AlN(2)/InN(2) superlattices with [001] growth direction. For all systems, the results are shown only up to 5 THz (i.e., within the acoustic range) and the lowest acoustic gaps (TA1 and LA1) are indicated.

Ge(2)/Sn(2), GaAs(2)/AlAs(2), and AlN(2)/InN(2) along the growth direction [001].

By symmetry, transverse branches along the [001] direction are twofold degenerate in bulk cubic semiconductors as well as in superlattices. The superlattice formation opens gaps in the TA and LA branches. Odd- and even-numbered gaps appear at the zone edge and zone center, respectively. We can denote these polarization gaps as TAj and LAj, with j taking appropriate odd and even numbers. The lowest polarization gaps, TA1 and LA1, have been highlighted in Fig. 2. For all the $A(2)/B(2)$ superlattices in Fig. 2, the lowest longitudinal gap LA1 coincides with a transverse gap (a gap higher than TA1 but lying within the acoustic-optical region). This clearly indicates that all these ultrathin superlattices are one-dimensional (1D) phononic systems, with a clear full phonon frequency gap in the [001] direction. For Si(2)/Ge(2) and GaAs(2)/AlAs(2), the clear gap occurs at 2.64 and 2.34 THz, respectively. The size of polarization gaps, as well as of the clear full gap, increases with increase in mismatch between the two constituent materials of a superlattice, both in terms of force constants and masses. The largest contributing factor for increase in the gap size is the mass difference between the materials A and B. This can be clearly seen by comparing the results for the three IV/IV superlattices and noting that, while the force constant difference between Si, Ge, and Sn is smaller than 15%, the mass ratios are $M(\mathrm{Si}) : M(\mathrm{Ge}) : M(\mathrm{Sn}) = 1.0 : 2.7 : 4.2$. It has also been shown in our previous work[18] that the gap locations vary inversely with the superlattice period. Consistent with this, Fig. 1 shows clearly that Si(19)/Ge(5) shows a frequency gap at a much lower frequency than that for Si(2)/Ge(2). It is also worth noting that this gap is smaller than in the Si(2)/Ge(2) case. It should be pointed out that, for all the systems studied here, no polarization gaps are found for the phonon wave vector pointing orthogonal to the growth direction. This, therefore, clarifies that these superlattices are 1D phononic systems. It is also readily apparent from Figs. 1 and 2 that the formation of the gaps reduces the group velocity of phonon modes in the direction of growth. In the plane perpendicular to the growth direction (which we will call the *layer plane*), very little group-velocity reduction is observed for all phonon modes. As one changes direction from the *layer plane* to the growth direction, the phonon mode velocities are slowly reduced.

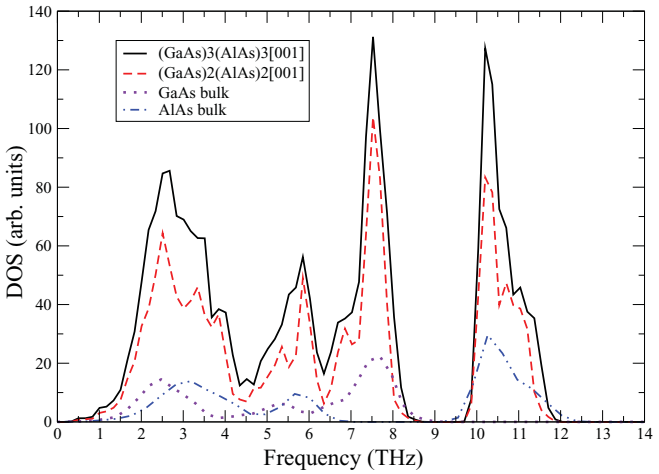

FIG. 3. (Color online) Phonon density of states for the GaAs(2)/AlAs(2) superlattice, GaAs(3)/AlAs(3) superlattice, GaAs bulk, and AlAs bulk.

The branch-folding and gap-opening effects upon superlattice formation create additional van Hove singularities in the phonon density of states not present in either constituent material. This can be appreciated from an inspection of Fig. 3, in which we present the density of states for the $(GaAs)_2(AlAs)_2[001]$ superlattice, the $(GaAs)_3(AlAs)_3[001]$ superlattice, and the GaAs and AlAs bulk. Some of the peaks due to the superlattice formation occur close to frequencies 0.5, 1, 4, 4.5, 5.5, 7, 10.5, and 11 THz. These new singularities correlate with the near zero-group velocities of the phonon modes at the edge of each polarization gap.

B. Embedded nanowires

As a second type of acoustic metamaterials, we consider Ge and Sn nanowires embedded in Si host. Layers of Si/Sn (Ref. 25) and Ge/Sn (Ref. 26) have successfully been grown using modern growth techniques. This suggests that embedded Ge/Si and Sn/Si nanowire structures are realizable in practice. In this work, we considered Ge and Sn nanowires along [001] and of cross-section area 0.27 nm × 0.27 nm embedded in a cubic Si host of period 5.43 nm. The phonon dispersion results for these systems are shown in Fig. 4.

The Ge nanowire exhibits a clear gap centered around 0.55 THz along the [110] symmetry direction, and is a 1D phononic system. The Sn nanowire is also a 1D phononic system with a clear gap at 0.5 THz but, unlike in the previous system, this gap extends across nearly the entire x-y plane, resulting in an almost two-dimensional (2D) phononic system with a thin region of transmission in the [100] direction. We have not incorporated atomic relaxation for any of the systems considered in this work. Consideration of this effect will be quite pronounced for the Sn nanowire system, as the atomic sizes of Sn and Si are quite different. We anticipate, due to this, a clear gap opening at the zone edge along the [100] direction, thus making the Sn nanowire a 2D phononic system. Another important result obtained is related to the location and size of the gap at the zone edge along [110]. The gap location for the Sn nanowire is at a lower frequency, and the size of the gap is much bigger, than that for the Ge nanowire. These variations are mainly due to the higher ghost (host) mass ratio of 4.23 for Sn/Si than 2.58 for Ge/Si and is an expected general result for acoustic metamaterials.

III. PHONON SCATTERING RATES

The main sources of phonon scattering in undoped bulk semiconductors are sample size (boundary effects), impurities, defects, and anharmonicity. Growth of nanostructured systems consisting of two or more different materials leads to at least two additional sources of phonon scattering: diffusion or mixing of atoms across interfaces and strain-induced dislocations or missing bonds at interfaces. Application of Fermi's golden rule is the usual procedure to estimate the lifetime for different phonon modes from these scattering mechanisms. Expressions for phonon relaxation rates in bulk materials due to boundaries, defects, and dopant-related carriers have been derived and are well documented.[27,28] Although detailed full-scale expressions for anharmonic relaxation rates due to three-phonon normal and umklapp processes, based upon considerations of the isotropic continuum model, are also available,[28] these have not been widely employed in calculations of lattice thermal

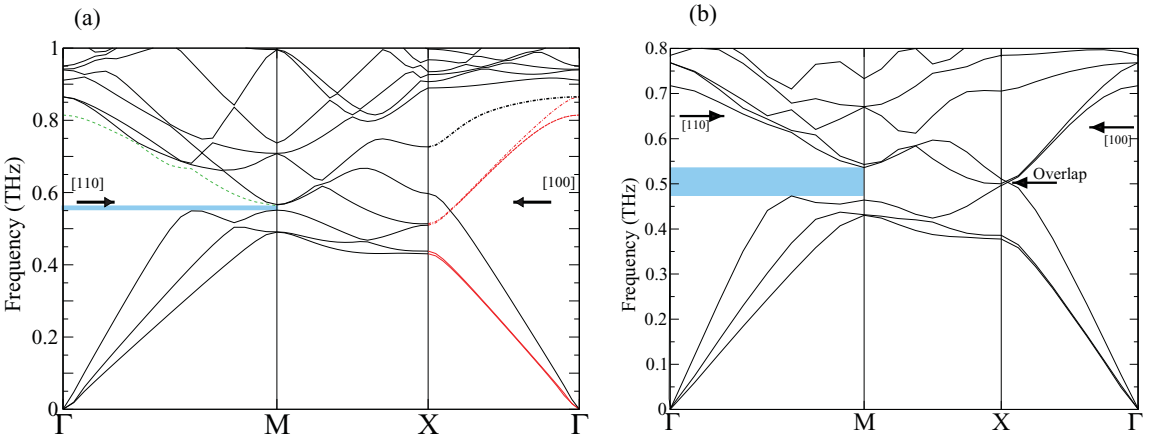

FIG. 4. (Color online) Phonon dispersion curves for (a) a Ge nanowire embedded in Si host and (b) a Sn nanowire embedded in Si host. Both nanowires extend along [001], have cross-section area 0.27 nm × 0.27 nm, and are embedded in a cubic Si host of period 5.43 nm.

conductivity. Most researchers have ignored the contribution from three-phonon normal (momentum-conserving) processes and have employed grossly oversimplified expressions, containing adjustable parameters, for umklapp (momentum-nonconserving) scattering rate (see, e.g., Ref. 29).

In this paper, we present an atomic-scale theory of phonon scattering rates due to mass defects, interface mixing, interface dislocation (in the form of missing atomic bonds), and anharmonic normal and umklapp processes in $A(m)/B(n)$ superlattices. We consider the total number of atoms in the system as $N+M=N_0(m+n)$, where N_0 represents the number of unit cells in the system. Also, for the ith atom, M_i and $\boldsymbol{v}_i$ are the mass and velocity, respectively, and for the ith atomic bond, $\boldsymbol{u}_i$ and K_i are the relative displacements and spring constants between atoms, respectively.

A. Scattering by mass defect

The scattering rate of a phonon mode $\boldsymbol{q}s$ (of wave vector $\boldsymbol{q}$ and polarization s) due to isotopic mass defects within each of the A and B materials of the superlattice $A(m)/B(n)$ is expressed, following the traditional theory,[30] as

$$\tau_{\mathrm{MD}}^{-1}[\omega(\boldsymbol{q}s)]=\frac{\Gamma\pi}{6N_0}\omega^2(\boldsymbol{q}s)g[\omega(\boldsymbol{q}s)], \tag{2}$$

where $g[\omega(\boldsymbol{q}s)]$ is the density of states for the mode and Γ is the isotopic mass parameter

$$\Gamma=L_f\Gamma(A)+(1-L_f)\Gamma(B), \tag{3}$$

with $L_f=m/(n+m)$ as the fractional size of the constituent material A. We express the isotopic mass parameter $\Gamma(i)$ for the ith material as

$$\Gamma(i)=\sum_j\frac{f_{i,j}f_{i,k}(M_{i,j}+M_{i,k}-2\bar{M}_i)}{(2\bar{M}_i)^2}, \tag{4}$$

with $f_{i,j}$ being the fraction of the jth isotope in the ith material and $\bar{M}_i$ as the average atomic mass.

B. Scattering by mass mixing across interfaces

We express the perturbed Hamiltonian of the $A(m)/B(n)$ superlattice system with interface mass mixing (IMS) as

$$\begin{aligned}H'(\mathrm{IMS})=&\frac{1}{2}\sum_{i=1}^{N}(M_i|\mathbf{v_i}|^2-M_A|\mathbf{v_A}|^2)\\&+\frac{1}{2}\sum_{i=N+1}^{N+M}(M_i|\mathbf{v_i}|^2-M_B|\mathbf{v_B}|^2)\end{aligned} \tag{5}$$

at the interfaces. From the application of Fermi's golden rule, we derive the following expression[6] for the scattering rate of a phonon $\boldsymbol{q}s$:

$$\begin{aligned}\tau_{\mathrm{IMS}}^{-1}(\boldsymbol{q}s)=&\frac{\alpha\pi}{2N_0(n+m)^2}\int d\omega(\boldsymbol{q}'s')g[\omega(\boldsymbol{q}'s')]\omega(\boldsymbol{q}s)\omega(\boldsymbol{q}'s')\\&\times\frac{\bar{n}(\boldsymbol{q}'s')+1}{\bar{n}(\boldsymbol{q}s)+1}\delta[\omega(\boldsymbol{q}s)-\omega(\boldsymbol{q}'s')]\\&\times\left[\left(1-\frac{e_Ae'_A}{e_Be'_B}\right)^2+\left(1-\frac{e_Be'_B}{e_Ae'_A}\right)^2\right],\end{aligned} \tag{6}$$

where α is regarded as a parameter related to the amount of mixing within three atomic layers on each side of the interface, $\bar{n}_{\boldsymbol{q}s}$ is the Bose-Einstein distribution of phonon mode $\omega(\boldsymbol{q}s)$ at temperature T, and e_B/e_A is the ratio of the amplitudes of eigenvectors of the mode $\omega(\boldsymbol{q}s)$ in materials B and A.

We employ the diatomic linear chain model to express the amplitude ratio e_B/e_A along the superlattice growth direction as

$$\frac{e_B}{e_A}=\frac{\left[\frac{1}{M_0}-\Delta\left(\frac{1}{M}\right)\right]\cos(l_zq_z)}{\left\{\left(\frac{1}{M_0}\right)^2\cos^2(l_zq_z)+\left[\Delta\left(\frac{1}{M}\right)\right]2\sin^2(l_zq_z)\right\}^{\frac{1}{2}}-\Delta\left(\frac{1}{M}\right)}, \tag{7}$$

with $M_0=\frac{1}{2}(1/M_A+1/M_B)$, $\Delta(1/M)=\frac{1}{2}(1/M_A-1/M_B)$, and l_z as the period along the superlattice growth direction. The ratio of amplitudes increases in magnitude with increasing wave vector q_z.

C. Scattering by dislocation at interfaces

The phonon scattering rate by dislocations has traditionally been derived by regarding the crystal as an elastic continuum (see, e.g., Ref. 27). Here, we use the atomic-scale terminology and consider a dislocation as a series of randomly missing bonds located near the interface, and write the perturbed Hamiltonian as

$$\begin{aligned}H'(\mathrm{IDS})=&\frac{1}{2}\sum_{i=1}^{N'}(K_0|\mathbf{u_i}|^2-K_A|\mathbf{u_A}|^2)\\&+\frac{1}{2}\sum_{i=N'+1}^{N'+M'}(K_0|\mathbf{u_i}|^2-K_B|\mathbf{u_B}|^2),\end{aligned} \tag{8}$$

where K_A (K_B) represents the interatomic spring constant in the layer A (B), $N'+M'$ is the total number of atomic bonds, and K_0 represents a spring constant in the dislocation region (i.e., has a value equal to zero, or close to zero, for missing or broken bonds). We further assume, for the present purpose, similar spring constants in the layers A and B (i.e., $K_A\approx K_B$).

Following the procedure for IMS, we have derived the following expression[6] for phonon relaxation due to interface dislocation scattering (IDS):

$$\begin{aligned}\tau_{\mathrm{IDS}}^{-1}(\boldsymbol{q}s)=&\frac{\pi\omega_0^4}{4N_0}\frac{\alpha'}{(n+m)^2}\int d\omega(\boldsymbol{q}'s')\frac{g[\omega(\boldsymbol{q}'s')]}{\omega(\boldsymbol{q}s)\omega(\boldsymbol{q}'s')}\\&\times\frac{\bar{n}(\boldsymbol{q}'s')+1}{\bar{n}(\boldsymbol{q}s)+1}\delta[\omega(\boldsymbol{q}s)-\omega(\boldsymbol{q}'s')]\\&\times\left[1+\left(\frac{e_Ae'_A}{e_Be'_B}\right)^2+1+\left(\frac{e_Be'_B}{e_Ae'_A}\right)^2\right],\end{aligned} \tag{9}$$

where α' is a measure of dislocation concentration, ω_0 can be approximated as the highest zone-center frequency, and the rest of the symbols have their usual meaning. The expression for the amplitude ratio e_B/e_A is already given in Eq. (7).

D. Anharmonic scattering

A formal atomic-scale expression for cubic anharmonicity in crystal potential V_3 is available in the literature.[27,28]

Upon this basis, including phonon oscillation amplitude terms explicitly, we express V_3 as

$$V_3 = \frac{1}{3!}\sum_{\boldsymbol{q}s,\boldsymbol{q}'s',\boldsymbol{q}''s''}(a^{\dagger}_{\boldsymbol{q}s} - a_{-\boldsymbol{q}s})(a^{\dagger}_{\boldsymbol{q}'s'} - a_{-\boldsymbol{q}'s'})(a^{\dagger}_{\boldsymbol{q}''s''} - a_{-\boldsymbol{q}''s''})\Psi(\boldsymbol{q}s,\boldsymbol{q}'s',\boldsymbol{q}''s'')\delta_{\boldsymbol{G},\boldsymbol{q}+\boldsymbol{q}'+\boldsymbol{q}''}, \tag{10}$$

where

$$\Psi(\boldsymbol{q}s,\boldsymbol{q}'s',\boldsymbol{q}''s'') = \frac{i}{\sqrt{N_0\Omega}}\sum_{\substack{\boldsymbol{b}\boldsymbol{b}'\boldsymbol{b}''\\ \alpha\beta\gamma}}\left(\frac{\hbar^3}{8M_bM_{b'}M_{b''}\omega(\boldsymbol{q}s)\omega(\boldsymbol{q}'s')\omega(\boldsymbol{q}''s'')}\right)^{1/2}\Psi_{\alpha\beta\gamma}(\boldsymbol{q}\boldsymbol{b},\boldsymbol{q}'\boldsymbol{b}',\boldsymbol{q}''\boldsymbol{b}'')e_{\alpha}(\boldsymbol{b}|\boldsymbol{q}s)e_{\beta}(\boldsymbol{b}'|\boldsymbol{q}'s')e_{\gamma}(\boldsymbol{b}''|\boldsymbol{q}''s''), \tag{11}$$

with Ω representing the unit-cell volume and $e(\boldsymbol{b}|\boldsymbol{q}s)$, etc., representing the polarization vectors. The Fourier components of the third-order interatomic force constant tensor $\Psi(\boldsymbol{q}\boldsymbol{b},\boldsymbol{q}'\boldsymbol{b}',\boldsymbol{q}''\boldsymbol{b}'')$ can be expressed as

$$\Psi(\boldsymbol{q}\boldsymbol{b},\boldsymbol{q}'\boldsymbol{b}',\boldsymbol{q}'',\boldsymbol{b}'') = \sum_{\boldsymbol{h}',\boldsymbol{h}''}\Psi(\boldsymbol{0}\boldsymbol{b},\boldsymbol{h}'\boldsymbol{b}',\boldsymbol{h}''\boldsymbol{b}'')e^{i\boldsymbol{q}'\cdot\boldsymbol{h}'}e^{i\boldsymbol{q}''\cdot\boldsymbol{h}''}, \tag{12}$$

where $\Psi(\boldsymbol{0}\boldsymbol{b},\boldsymbol{h}'\boldsymbol{b}',\boldsymbol{h}''\boldsymbol{b}'')$ is the third-order interatomic force constant tensor, and $\boldsymbol{h}'$ and $\boldsymbol{h}''$ are lattice translation vectors for the superlattice structure.

Following the notation in Ref. 28, we express the phonon relaxation rate due to three-phonon processes as

$$\begin{aligned}\tau^{-1}(\boldsymbol{q}s) = {}& \frac{\pi\hbar\rho_{av}^2\gamma^2}{N_0\Omega\bar{c}^2}\sum_{\boldsymbol{q}'s',\boldsymbol{q}''s'',\boldsymbol{G}}\omega(\boldsymbol{q}s)\omega(\boldsymbol{q}'s')\omega(\boldsymbol{q}''s'')DM(\boldsymbol{q}s,\boldsymbol{q}'s',\boldsymbol{q}''s'')\\ &\times\left\{\left[\frac{\bar{n}(\boldsymbol{q}'s')[\bar{n}(\boldsymbol{q}''s'')+1]}{\bar{n}(\boldsymbol{q}s)+1}\delta[\omega(\boldsymbol{q}s)+\omega(\boldsymbol{q}'s')-\omega(\boldsymbol{q}''s'')]\delta_{\boldsymbol{q}+\boldsymbol{q}',\boldsymbol{q}''+\boldsymbol{G}}\right]\right.\\ &\left.+\left[\frac{1}{2}\frac{\bar{n}(\boldsymbol{q}'s')\bar{n}(\boldsymbol{q}''s'')}{\bar{n}(\boldsymbol{q}s)}\delta[\omega(\boldsymbol{q}s)-\omega(\boldsymbol{q}'s')-\omega(\boldsymbol{q}''s'')]\delta_{\boldsymbol{q}+\boldsymbol{G},\boldsymbol{q}'+\boldsymbol{q}''}\right]\right\},\end{aligned} \tag{13}$$

where ρ_{av} is the average mass density, $\bar{c}$ is the average acoustic velocity, γ is the Grüneisen constant for the joint system, $\boldsymbol{G}$ is a reciprocal lattice vector, and $\mathrm{DM}(\boldsymbol{q},\boldsymbol{q}',\boldsymbol{q}'')$ is the *dual mass term* (DMT) arising from the presence of two materials in the superlattice.[31] The DMT can be expressed as

$$\begin{aligned}\mathrm{DM}(\mathbf{q},\mathbf{q}',\mathbf{q}'') = \frac{1}{64}\left\{\frac{1}{2\rho_A^{\frac{3}{2}}}\left[1+\frac{\rho_A^{\frac{1}{2}}}{\rho_B^{\frac{1}{2}}}\left(\frac{e_B}{e_A}+\frac{e'_B}{e'_A}+\frac{e''_B}{e''_A}\right)+\frac{\rho_A}{\rho_B}\left(\frac{e_Be'_B}{e_Ae'_A}+\frac{e'_Be''_B}{e'_Ae''_A}+\frac{e_Be''_B}{e_Ae''_A}\right)+\frac{\rho_A^{\frac{3}{2}}}{\rho_B^{\frac{3}{2}}}\left(\frac{e_Be'_Be''_B}{e_Ae'_Ae''_A}\right)\right]\right.\\ \left.+\frac{1}{2\rho_B^{\frac{3}{2}}}\left[1+\frac{\rho_B^{\frac{1}{2}}}{\rho_A^{\frac{1}{2}}}\left(\frac{e_A}{e_B}+\frac{e'_A}{e'_B}+\frac{e''_A}{e''_B}\right)+\frac{\rho_B}{\rho_A}\left(\frac{e_Ae'_A}{e_Be'_B}+\frac{e'_Ae''_A}{e'_Be''_B}+\frac{e_Ae''_A}{e_Be''_B}\right)+\frac{\rho_B^{\frac{3}{2}}}{\rho_A^{\frac{3}{2}}}\left(\frac{e_Ae'_Ae''_A}{e_Be'_Be''_B}\right)\right]\right\}^2,\end{aligned} \tag{14}$$

where ρ_A and ρ_B are the mass densities of the materials A and B, respectively. Once again, we use Eq. (7) to express the ratio of the amplitudes of oscillation e_B/e_A along the superlattice growth direction using the diatomic chain model.

E. Numerical procedure

For numerical calculations of the phonon relaxation rates from the various scattering processes discussed in the previous sections, we adopted the following procedure. The Brillouin zone summation of a function $f(\boldsymbol{q}s)$ was carried out using the concept of special $\boldsymbol{q}$ points.[32] Accordingly, we expressed

$$\sum_{\boldsymbol{q}} f(\boldsymbol{q}s) = N_0\sum_{j=1}^{N_{\mathrm{sp}}} W_j f(\boldsymbol{q}_j s), \tag{15}$$

where N_{sp} is the number of special points within the first Brillouin zone, the functions $\{f(\boldsymbol{q}_j s)\}$ [which are functions of phonon frequencies $\{\omega(\boldsymbol{q}_j s)\}$] were evaluated for a set $\{\boldsymbol{q}_j\}$ of special phonon wave vectors from the lattice dynamical calculation described in Sec. II, and $W(\boldsymbol{q}_j)$ is the non-negative weight factor associated with a special point $\boldsymbol{q}_j$. The momentum-conservation conditions $\boldsymbol{q}+\boldsymbol{q}'\pm\boldsymbol{q}''=\boldsymbol{G}$ were expressed as

$$\begin{aligned}|q_x+q'_x\pm q''_x-G_x| &\leqslant \Delta_1,\\ |q_y+q'_y\pm q''_y-G_y| &\leqslant \Delta_2,\\ |q_z+q'_z\pm q''_z-G_z| &\leqslant \Delta_3,\end{aligned} \tag{16}$$

with Δ_i chosen as the smallest $|q_i|$ in the set of special wave vectors. It was sufficient to consider only the first- and second-shell reciprocal lattice vectors $\{\boldsymbol{G}_i\}$ when dealing with three-phonon umklapp processes. The Dirac delta functions energy conservation conditions were expressed in Gaussian form using

$$\delta(x) = \lim_{\epsilon\to 0}\frac{1}{\epsilon\sqrt{\pi}}\exp(-x^2/\epsilon^2). \tag{17}$$

F. Effect of metamaterial formation on relaxation rates

From the formulas presented in Sec. III, it is clear that the phonon relaxation rates due to the IMS, IDS, and anharmonicity depend on several factors, including the amplitude ratio e_B/e_A, phonon frequency, superlattice period, the interface parameters α and α', and the anharmonicity parameter γ. Among these parameters, the amplitude ratio e_B/e_A varies most sensitively with the phonon wave vector q_z along the metamaterial growth direction: while e_B/e_A is unity at the zone center, it rises toward infinity at the zone edge ($l_z q_z = \pi/2$). We can make a few qualitative statements regarding phonon relaxation rates from different scattering sources.

We can expect that interfaces will weakly scatter long-wavelength modes. For phonon modes near the zone edge in the growth direction, the two layers (i.e., the two material regions) in each superlattice unit cell will act out of phase and, hence, traveling phonons will be scattered more strongly by the presence of the interfaces. For both IMS and IDS scattering mechanisms, optical modes in superlattices will be scattered at the interface more strongly than acoustic modes. Sharp peaks in the density of states in the optical range, due to strongly confined modes with much reduced velocities, will result in the scattering rate of optical modes being greater than for their acoustic counterparts. The factor $1/(n+m)^2$ in Eqs. (7) and (9) implies that phonon interface scatterings (IMS and IDS) are greatest for thin superlattices and decrease as the superlattices become thicker. The parameter α in Eq. (9) gives an indication of the amount of mixing that occurs at the interface, and is expected to increase with increasing period, but not by a dramatic amount. The parameter α' in Eq. (9) indicates the number of dislocations and distortions of the crystal at the interfaces and is also proportional to interface area. The ratio of α and α' gives a clear indication of the interface quality and dominant type of disorder present.

We will consider three-phonon interactions to emphasize the effect of metamaterial formation on phonon relaxation rates. Figure 5(a) shows the room-temperature three-phonon relaxation rates of various phonon modes in the Si(0.543 nm)/Ge(0.543 nm)[001] superlattice. For comparison, we show in Fig. 5(b) a similar set of relaxation-rate curves for the fictitious superlattice of the same periodicity with $\mathrm{DM} = 1/\rho_{av}^3$. The first and clearest feature to notice is that the relaxation rate of almost all of the phonon modes is increased in the real superlattice structure compared to its fictitious bulk counterpart. This increase in the relaxation rate is directly a result of the DMT. For easy comparison, we note that, for the longitudinal acoustic branch, the ratio of $\tau^{-1}_{s=\mathrm{LA,SiGe}}$ with $[\tau^{-1}_{s=\mathrm{LA,Si}} + \tau^{-1}_{s=\mathrm{LA,Ge}}]/2$ is 2.28 at $X/2$.

There are two contributing factors inside the DMT that lead to the increase in the phonon relaxation rate: the amplitude ratio e_B/e_A and the density ratio ρ_A/ρ_B (or, the mass ratio M_A/M_B). As mentioned earlier, toward the edge of the Brillouin zone, the ratio e_B/e_A grows exponentially, leading to a much greater increase in the relaxation rate for zone-edge modes compared to zone-center modes. For bulk materials and the fictitious bulk superlattice, the exponential rise in the relaxation rate does not occur at the zone edge.

In general, for superlattice systems, the relaxation rate of the lowest-lying acoustic modes increases with an increase in wave vector $\mathbf{q}$ (due to ω increasing with $\mathbf{q}$). This increase is also observed in bulk materials for the same reason. From Γ to X, the relaxation rate of the folded acoustic branches decreases with wave vector, which is due to two bulklike features. These are as follows: (i) smaller decrease in frequency with increasing wave vector and (ii) folded zone-edge modes have fewer decay routes than the zone-center folded modes. For optical modes, the phononic properties (i.e., the gap) of the system become more important in addition to the DMT. If one ignores the effects of DMT for a moment, the effects of gap formation and band splitting can be considered more clearly. In bulk systems, for phonon modes at the zone edge X, there exists only one available phonon energy (for a particular phonon polarization), whereas in a phononic crystal, this mode energy is split and, hence, there are two possible energies to satisfy the energy conservation law. Initially, this would lead one to believe that there would be a slight increase in the number of allowed interactions and, hence, a slight increase in the relaxation rate in general. This is not true, as the effect of creating a band gap is to reduce the number of allowed interactions (due to the stop bands and energy gaps) and hence the relaxation rate, if only these factors were taken into account, would appear to be reduced by up

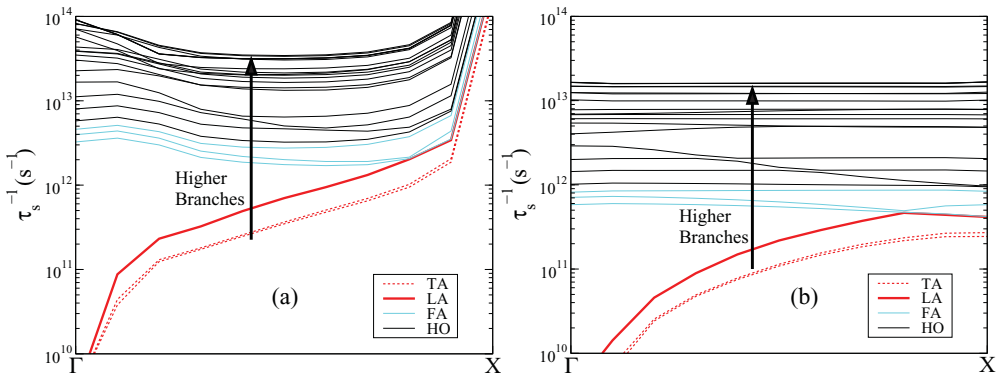

FIG. 5. (Color online) Three-phonon relaxation rates at 300 K for (a) the Si(0.543 nm)/Ge(0.543 nm)[001] superlattice; (b) a fictitious Si(0.543 nm)/Ge(0.543 nm)[001] superlattice for which the relaxation rate was calculated using the average density of Si and Ge. The results for the three acoustic branches [longitudinal (LA) and two transverse (TA)] are shown in dark grey (red online) and the folded branches (FA) are shown in light grey (blue online). The highest optical branches (HO) are also highlighted.

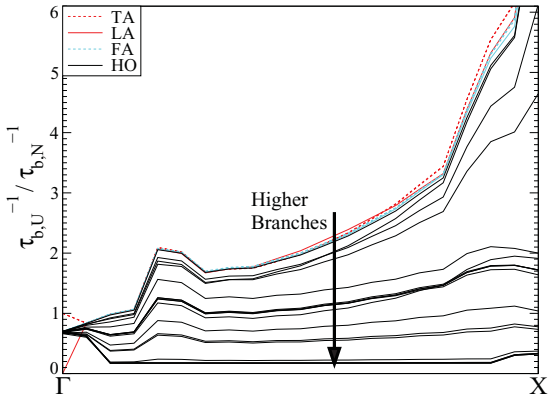

FIG. 6. (Color online) The ratio of three-phonon umklapp and normal scattering rates at 300 K in the Si(0.543 nm)/Ge(0.543 nm)[001] superlattice for various phonon branches with modes across the Brillouin zone along the growth direction.

to 10% compared to the bulk results. However, this effect is overshadowed by the dominant DMT, which creates an effective increase in the relaxation rate. Comparison of the fictitious bulk superlattice with the average relaxation rate of Si and Ge {that is, $[\tau_{\mathrm{Si}}^{-1}(\mathbf{q},b) + \tau_{\mathrm{Ge}}^{-1}(\mathbf{q},b)]/2$} confirms this result. The effect of DMT is by far the most important and dominant feature and is, in effect, due to the two-layer nature of the system.

The larger periodicity along the growth direction leads to the participation of shorter reciprocal lattice vectors ($\boldsymbol{G}$) for umklapp processes in superlattices than in bulk materials. The combination of superlattice periodicity and the DMT results in a more dramatic effect for three-phonon umklapp processes than their normal-processes counterparts. Figure 6 shows the relaxation-rate ratio between the umklapp processes and normal processes for phonon modes. Clearly, for acoustic modes, normal and umklapp processes have comparable contributions near the zone center, but umklapp processes become increasingly dominant toward the zone edge. This is the same as in bulk materials. At the zone edge, the ratio decreases for higher branches: for example, at 300 K, the highest optical modes are dominated by normal processes. By comparing the results for the real superlattice with the bulk materials and the fictitious bulk superlattice, we can draw two conclusions: (i) The DMT increases the ratio $\tau_{s,U}^{-1}/\tau_{s,N}^{-1}$ by approximately 2 to 4 across the Brillouin zone (excluding the zone edge X). This is because umklapp processes tend to involve longer wave vectors than normal processes, which means the amplitude ratio in the DMT is greater for these processes. This also explains the exponential growth in Fig. 6 at the zone edge as $\frac{e_B}{e_A} + \frac{e_A}{e_B}$ tends to infinity. (ii) The gaps in the dispersion relations lead to little noticeable change in the ratio $\tau_{s,U}^{-1}/\tau_{s,N}^{-1}$.

IV. SPECIFIC HEAT

The specific heat of a superlattice system is determined by three factors: atomic species of the constituent materials, its period, and the relative thicknesses of the constituent material layers within a unit cell. Here, we use our numerical results to present a study of each of these factors.

A. Material constituents

In Fig. 1, we presented the phonon dispersion of a few ultra thin $A(m)/B(n)$ superlattices. In Fig. 7, we present the specific-heat capacity C_v of these structures as a function of temperature. It is worth emphasizing that these superlattice structures consist of the same period and have equal number of layers of materials A and B. We can clearly observe three features for all the superlattices presented: (i) C_v increases as T^3 at low temperatures, as one would expect for bulk systems; (ii) the C_v for each superlattice is slightly lower than the average of the two bulk materials; and (iii) the denser the material (i.e., the higher the mass density), the lower the specific heat. None of these features are unexpected and are what one would predict from a simple Debye-type model.

B. Superlattice periodicity

Figure 8 shows the results for the specific heat of the GaAs(2)/AlAs(2)[001] and GaAs(3)/AlAs(3)[001] superlattices. The first observation we make is that the result for the specific heat is practically identical for the two superlattices at all temperatures. This holds true for superlattices of greater period as long as the layer thicknesses of the materials A and B remain the same. We also find that the low-temperature (below 100 K) values of the specific heat of the superlattices are practically the same for either of the constituent bulk materials. This is not surprising, as at such temperatures, only phonons in the acoustic frequency range are significantly populated and that both GaAs and AlAs show similar frequency dispersion relations in the long-wavelength limit. At higher temperatures, the specific heat of the superlattices is slightly lower than the average of the two bulk values. For example, at 1000 K, the specific heat of the superlattices is approximately 3% smaller than the average of the bulk values.

C. Relative thicknesses of constituent material layers

In Fig. 9, we present the specific-heat capacity of a Si(20-n)/Ge(n)[001] superlattice as a function of temperature. We first note that, unlike GaAs and AlAs, the low-temperature values of C_v are different for bulk Si and Ge. Although the variation of C_v in the low-temperature regime for both Si and Ge is as T^3, Ge at low temperatures has a higher specific-heat capacity than Si. However, this behavior switches at around 60 K, and Si has a greater C_v than Ge. The specific-heat capacity of the Si(20-n)/Ge(n)[001] superlattices, regardless of the value of n, also is greater than C_v of Ge above 60 K.

It is interesting to note that the average of the specific-heat capacities of bulk Si and Ge lies between $n = 6$ and 8, but not the symmetric value $n = 10$. For example, at high temperatures, the specific-heat capacity (per kg) of the Si(10)/Ge(10) superlattice is approximately 14% below the average of the values for the bulk Si and Ge crystals.

V. THERMAL CONDUCTIVITY

For discussing the lattice thermal conductivity of metamaterials, we will employ the concept of *single-mode relaxation*

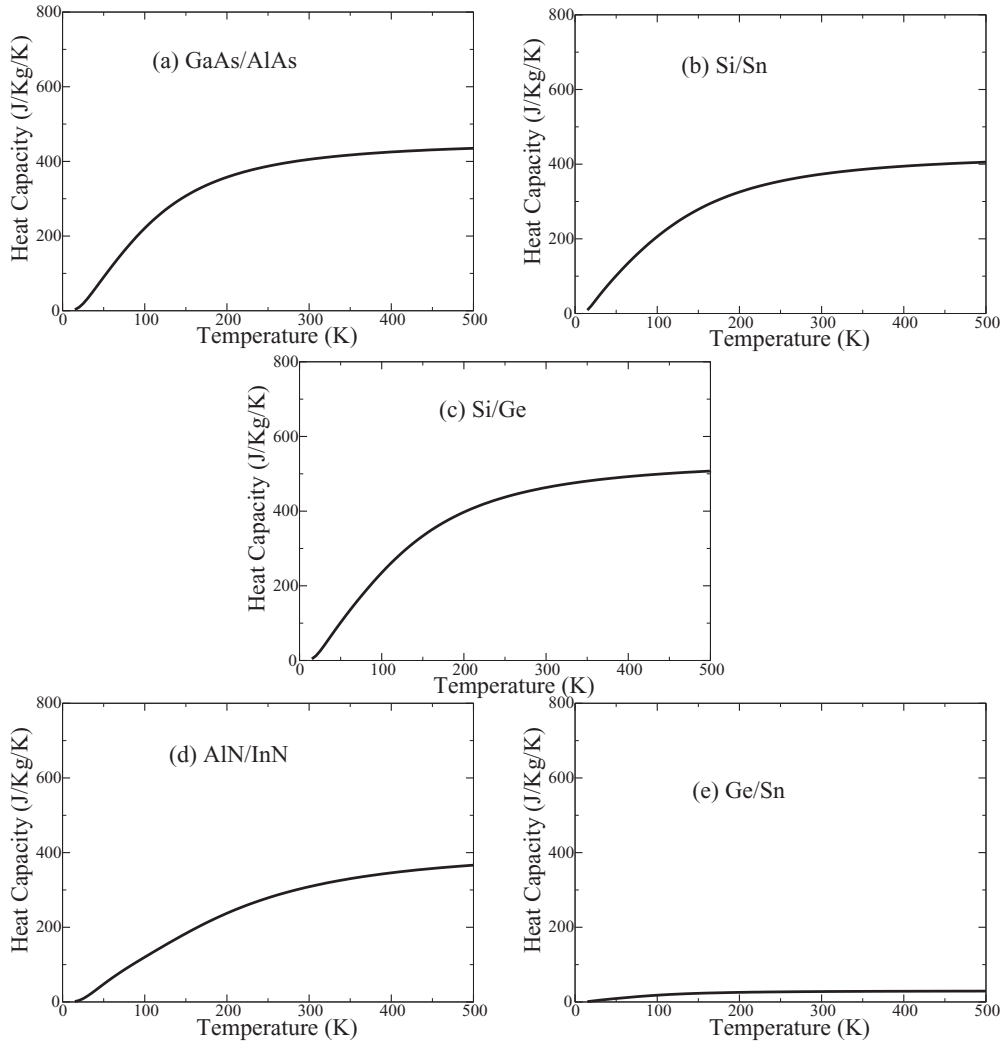

FIG. 7. Temperature variation of the lattice specific heat for the Si(2)/Sn(2), Ge(2)/Sn(2), GaAs(2)/AlAs(2), and AlN(2)/InN(2) superlattices with [001] growth direction.

time.[28,30] Within this concept, the expression for the thermal conductivity tensor can be expressed as

$$\kappa_{ij} = \frac{\hbar^2}{N_0 \Omega k_B T^2} \sum_{\boldsymbol{q},s} \omega^2(\boldsymbol{q}s) v_i(\boldsymbol{q}s) v_j(\boldsymbol{q}s) \tau(\boldsymbol{q}s) \bar{n}(\boldsymbol{q}s)[\bar{n}(\boldsymbol{q}s)+1]. \tag{18}$$

For numerical calculations of the conductivity tensor, we will perform the sum $\sum_{\boldsymbol{q}}$ over the Brillouin zone of the metamaterial. Such a sum will be carried out by utilizing the special $\boldsymbol{q}$-points scheme[32] in the same manner as discussed in Sec. III E. This thus requires calculations of phonon frequencies $\{\omega(\boldsymbol{q}_i s)\}$, phonon group velocities $\{\boldsymbol{v}(\boldsymbol{q}_i s)\}$, and phonon relaxation rates $\{\tau^{-1}(\boldsymbol{q}_i s)\}$ for a set of special points $\{q_i\}$ with weight factors $\{W(\boldsymbol{q}_i)\}$.

In view of the fact that the amount of interface mass mixing and the nature and density of broken bonds (or dislocations) at the interfaces are generally uncontrollable and not known with certainty, we treated α and α' as adjustable parameters. We also treated the anharmonicity coefficient γ as a mode-averaged and temperature-independent adjustable parameter.

A. Results for the Si/Ge[001] superlattices

We have applied our method to explain the low-temperature thermal conductivity of two Si/Ge superlattices: Si(19)/Ge(5)[001] and Si(72)/Ge(30)[001]. These SLs have been fabricated and their thermal conductivity measured by Lee *et al.*[24] In Fig. 10, we present the results of our numerical calculations for κ_{zz}, the conductivity of these SLs along the growth direction. As these are low-temperature results, phonon-phonon scattering is ignored ($\gamma = 0$). For the boundary scattering, the sizes of the samples are taken as the same as those measured by Lee *et al.*[24] and the scattering due to the isotopic mass defects is calculated *a priori* from the relative isotopic abundances.

For the thinner superlattice, for majority of phonon modes across the frequency spectrum, IMS is the dominant scattering mechanism and the contribution of IDS is negligible ($\alpha \approx 550$ and $\alpha' \approx 0.0$). This suggests that the relative number of dislocations is small and the quality of the interfaces between the layers of the thinner superlattice in Ref. 24 is relatively clean. This is further supported by other experimental studies,[33] which suggest that stable forms of thin

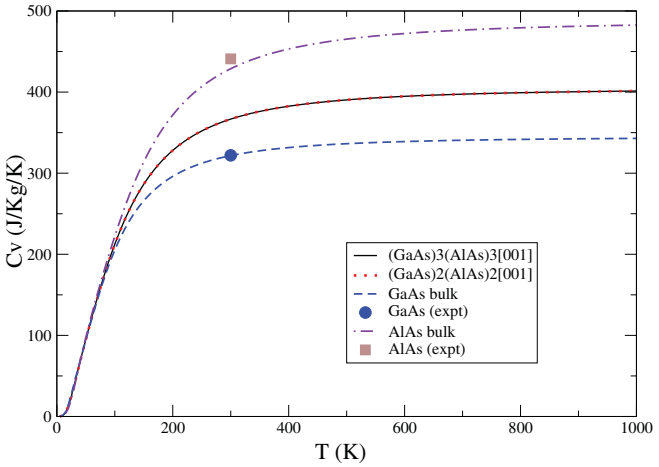

FIG. 8. (Color online) The lattice specific heat of ultrathin GaAs/AlAs[001] superlattices compared with the results for GaAs and AlAs bulk crystals.

Si/Ge superlattices can be fabricated without the presence of many interface dislocations or missing bonds. In contrast, for the thicker superlattice, the dominant scattering mechanism is IDS, indicating that the interfaces have several broken or distorted bonds (as $\alpha \approx 10^7$ and $\alpha' \approx 10^{-4}$). For large period superlattices, much of the region in each constituent material layer mimics its individual bulk lattice constant at the cost of increase in the strain at the interface due to lattice mismatch, thus leading to the development of a greater amount of dislocations and other defects or imperfections.

The interplay between the IMS and IDS in controlling the phonon lifetime in such superlattices is helpful in explaining the apparent collapse of the thermal conductivity measured by Lee *et al.* for superlattice period larger than approximately 70 Å. In essence, in samples with a small periodicity, the strain on the structure is very small, hence, the contribution from IDS will be very small. In contrast, samples of thicker periods (larger than 70 Å) are of poor quality. This is due to the

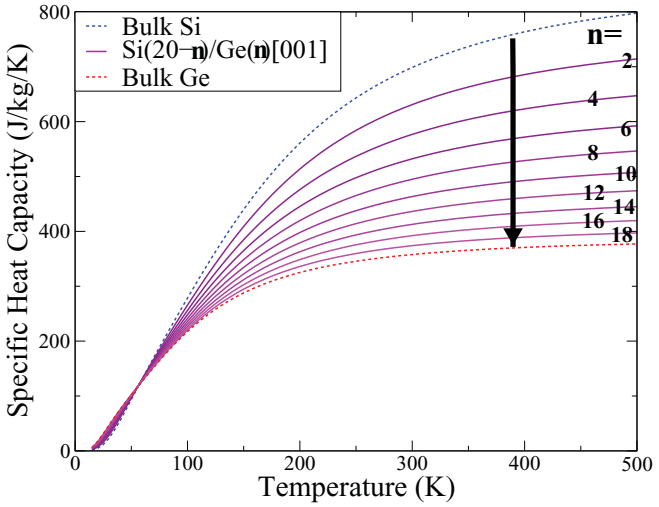

FIG. 9. (Color online) The lattice specific heat of Si(20-n)/Ge(n)[001] superlattices compared with the results for Si and Ge bulk crystals.

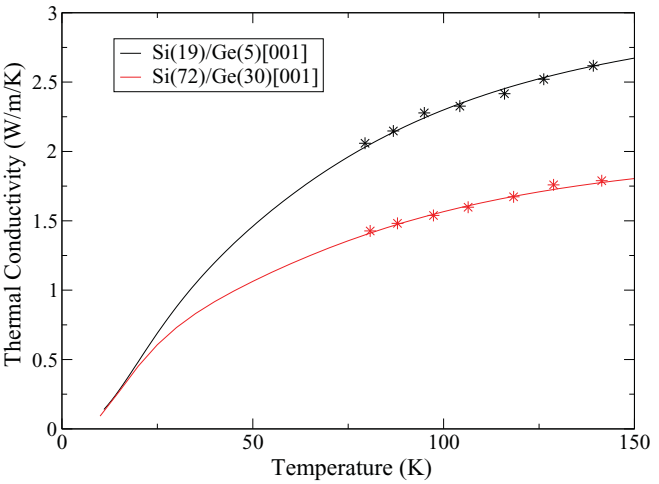

FIG. 10. (Color online) The thermal conductivity κ_{zz} of the Si(19)/Ge(5)[001] and Si(72)/Ge(30)[001] superlattices along the growth direction as a function of temperature. The lines are the theoretical fits and stars show the measured results from Lee *et al.* (Ref. 24).

total strain energy of the superlattice increasing with period, whereas the dislocation energy remains relatively constant leading to plastic deformation.[35] In the language of the present work, for thicker periods, the IDS contribution dramatically increases leading to the collapse of the conductivity. After this point, the contribution of IDS no longer increases as fast as the lifetime contribution decreases due to increasing period [see Eqs. (7) and (9)]. For much thicker superlattices (several microns in period), one anticipates the conductivity rising to the average of the two constituent material's bulk values. This is further verified below when discussing the results for GaAs/AlAs superlattices, where the two are lattice matched and IDS has no major contribution to play. Hence, for non-lattice-matched superlattice structures of large periodicity, IDS will result in a dip, or collapse, in thermal conductivity. In lattice-matched structures where only IMS is present, no such drop can be expected. This is evident from the measurements presented by Capinski *et al.*[34] for GaAs/AlAs superlattices.

The anisotropic behavior of the thermal conductivity upon superlattice formation can be appreciated from the results presented in Fig. 11. At low temperatures, the ratio κ_{zz}/κ_{xx} tends to unity for the thicker superlattice, whereas it remains much greater than unity for the thin superlattice. These behaviors can be explained. At low temperatures, only low-lying modes are populated. Thus, in the thicker superlattice, the large amounts of zone folding means that, at low temperatures, phonon modes both at the zone center and the zone edge are populated. Conversely, for thinner superlattices with less zone folding, the zone-edge modes are not populated until higher temperatures. As zone-edge modes are scattered more strongly than zone-center modes, both IDS and IMS become highly anisotropic scattering mechanisms at low temperatures for the thin superlattice, but less so for the thicker superlattice.

In the Introduction, we mentioned that the lattice thermal conductivity of a material can be controlled by three factors: the heat capacity, the phonon group velocity, and the phonon lifetime. The results presented here have clearly shown that

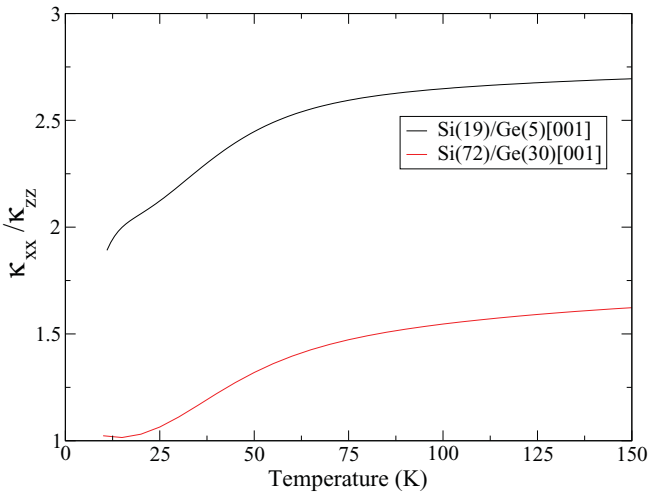

FIG. 11. (Color online) The thermal conductivity ratio κ_{xx}/κ_{zz} for the superlattices Si(19)/Ge(5)[001] and Si(72)/Ge(30)[001] as a function of temperature.

the formation of the superlattice structure has little or no effect on the heat capacity, and the phonon group velocity (while showing a reduction) is not the factor that is responsible for the largest reduction in the conductivity compared to the bulk systems. Hence, it is the phonon scattering by the interfaces due to the IMS and IDS mechanisms that is responsible for the low thermal conductivity for the Si/Ge superlattice samples fabricated and studied by Lee *et al.*[24]

B. Results for GaAs/AlAs[001] superlattices

In Fig. 12, we have plotted the variation of the thermal conductivity tensor components κ_{zz} and κ_{xx} for the GaAs(2)/AlAs(2)[001] superlattice. Also shown are the results of experimental measurements by Capinski *et al.*[34] of the conductivity along the growth direction κ_{zz} in the temperature range 100–400 K. An effective boundary length value of

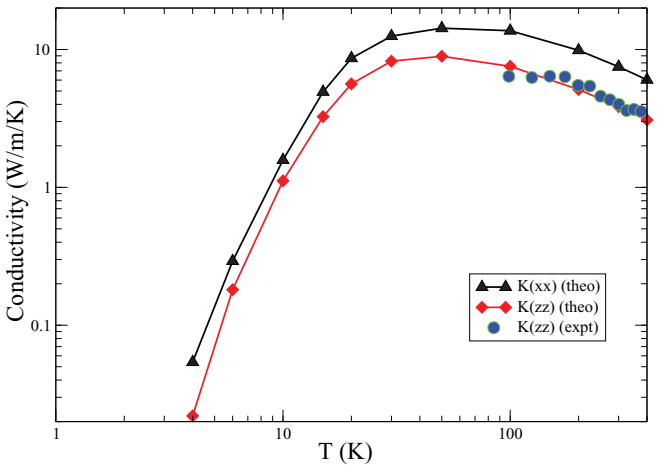

FIG. 12. (Color online) Temperature variation of the thermal conductivity components κ_{zz} and κ_{xx} for the GaAs(2)/AlAs(2)[001] superlattice. Theoretically calculated results are shown with symbols (squares and triangles) and lines, and the experimentally measured results from Capinski *et al.* (Ref. 34) are shown by filled blue circles.

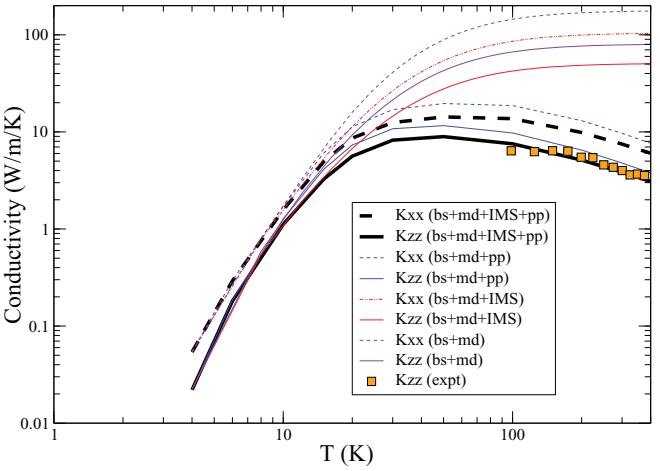

FIG. 13. (Color online) Role of different scattering processes in determining the thermal conductivity components κ_{zz} and κ_{xx} for the GaAs(2)/AlAs(2)[001] superlattice. The experimentally measured results from Capinski *et al.* (Ref. 34) are shown by the square symbols.

453 nm was considered, as given in the paper by Capinski *et al.*[34] The Grüneisen constant γ was set at 0.5. As GaAs and AlAs are much better lattice matched, the IDS was not considered and should not be necessary as there should be very few, if any, broken bonds. We also needed to consider a much smaller value of the interface mass diffusion parameter $\alpha = 0.01$ than that required for the Si/Ge superlattices. This is expected as much less mixing at the interface occurs in these lattice-matched materials. Our theoretical results also suggest that, at low temperatures, particularly below 10 K, boundary scattering becomes the dominant scattering mechanism. The relative roles of the boundary scattering, isotopic mass defect scattering, the IMS, the IDS, and anharmonic scattering can be appreciated from an inspection of the results presented in Fig. 13. In particular, the role of superlattice formation is crucial to understanding these results. The additional scattering mechanism (IMS) and the modification to the phonon-phonon scattering are clearly shown to be vitally important for describing the exceptionally low thermal conductivity of superlattice structures. The phonon-phonon interaction dominates the form of the temperature dependence, but on its own is insufficient to account for the magnitude. Likewise, the IMS can only account for very low temperature behavior and can not account for the observed decrease at high temperatures.

Apart from producing good agreement with the experimental results, our theoretical results suggest that the conductivity components exhibit a rather broad peak centered around 40 K. At room temperature and above, the in-plane component κ_{xx} is predicted to be almost twice the value of the growth-direction component κ_{zz}. At lower temperatures, this ratio is found to be slightly reduced. This indicates that an increase in the IMS and anharmonic scatterings is responsible for the larger difference in the in-plane and along-growth components of the conductivity. As discussed earlier, the GaAs/AlAs superlattices are latticed matched and, hence, the contribution due to IDS is small or negligible and thus there is no dip in thermal conductivity with superlattice period for the reason discussed earlier.

We have also performed calculations of the conductivity tensor for the GaAs(3)/AlAs(3)[001] superlattice. In agreement with the experimental measurement by Capinski *et al.*,[34] our calculations suggest that the conductivity of the (3,3) superlattice is larger than that of the (2,2) superlattice for all temperatures above the conductivity peak. In particular, at room temperature, our computed ratio of $\kappa_z z(3,3)/\kappa_{zz}(2,2) = 1.45$ is in good agreement with the ratio of 1.65 obtained from the experimental measurements.

VI. SUMMARY

In this paper, we have shown that the key component to understanding the thermal conductivity of nanostructured superlattices is the phonon scattering strength. In order to establish this point, we have discussed the contribution from relevant scattering mechanisms in such structures.

To start with, we have discussed a consistent theoretical approach for lattice dynamics (i.e., phonon dispersion relations) and thermal properties (e.g., specific heat and phonon conductivity) of acoustic metamaterials. Results of phonon dispersion curves have been presented for semiconductor metamaterials in the form of superlattices and also embedded nanowires. The presence of phonon polarization gaps, as well as clear phononic gaps, have been presented and discussed. Results have also been presented for lattice specific heat for superlattices and differences from bulk results identified.

Considering realistic phonon dispersion results, we have developed a theory of phonon scatterings from interface mass mixing, interface dislocation, and anharmonic interactions involving three-phonon normal and umklapp processes in acoustic metamaterials. The role of *dual mass term* and the formation of interfaces in controlling phonon lifetime and eventually lattice thermal conductivity has been carefully discussed. Using our theoretical results, we have successfully explained existing experimental measurements of the thermal conductivity of thin and thick Si/Ge[001] superlattices and ultrathin GaAs/AlAs[001] superlattices. It is found that, beyond 100 K, the conductivity of Si/Ge superlattices is largely controlled by interface mass mixing and dislocation effects and the thermal conductivity of thin GaAs/AlAs superlattices is largely controlled by anharmonic effects.

It is clear from the results for the Si/Ge and GaAs/AlAs samples that the dip in thermal conductivity of the non-lattice-matched superlattices is due to strain effects, whereas the thermal conductivity of lattice-matched samples do not show this feature. It is also readily apparent that, without the modification shown here to the phonon-phonon interaction, one can not explain the high-temperature dependence of the thermal conductivity in lattice-matched superlattices. The theory outlined in this paper can be applied, with suitable extension, to study the vibrational and thermal properties of many other forms of nanostructured acoustic metamaterials.

ACKNOWLEDGMENTS

S.P.H. was financially supported by the Leverhulme Trust (UK) through the Grant No. F/00 144/AS. G.P.S. is grateful to the Leverhulme Trust for the overall support of the project entitled Vibrational and Thermal Properties of Phononic Crystals.

*Present address: Department of Physics, University of Surrey, Guildford, Surrey, GU1 7XH, UK.

[1] L. Fock, M. Ambati, and X. Zhang, MRS Bull. **33**, 931 (2008).
[2] T. Gorishnyy, C. K. Ullal, M. Maldovan, G. Fytas, and E. L. Thomas, Phys. Rev. Lett. **94**, 115501 (2005).
[3] S. Yang, J. H. Page, Zhengyou Liu, M. L. Cowan, C. T. Chan, and P. Sheng, Phys. Rev. Lett. **93**, 024301 (2004).
[4] Y. Ezzahri, S. Grauby, J. M. Rampnoux, H. Michel, G. Pernot, W. Claeys, S. Dilhaire, C. Rossignol, G. Zeng, and A. Shakouri, Phys. Rev. B **75**, 195309 (2007).
[5] D. G. Cahill, W. K. Ford, K. E. Goodson, G. D. Mahan, A. Majumdar, H. J. Maris, R. Merlin, and S. R. Phillpot, J. Appl. Phys. **93**, 793 (2003).
[6] S. P. Hepplestone and G. P. Srivastava, Phys. Rev. B **82**, 144303 (2010).
[7] S. M. Rytov, Akust. Zh. **2**, 71 (1956) [Sov. Phys. Acoust. **2**, 68 (1956)].
[8] M. S. Kushwaha, P. Halevi, G. Martinez, L. Dobrzynski, and B. Djafari-Rouhani, Phys. Rev. B **49**, 2313 (1994).
[9] S. G. Walkauskas, D. A. Broido, K. Kemps, and T. L. Reinecke, J. Appl. Phys. **85**, 2579 (1999).
[10] W. Fon, K. C. Schwab, J. M. Worlock, and M. L. Roukes, Phys. Rev. B **66**, 045302 (2002).
[11] N. Mingo, Phys. Rev. B **68**, 113308 (2003).
[12] W. Liu and A. A. Balandin, J. Appl. Phys. **97**, 73710 (2005).
[13] P. G. Murphy and J. E. Moore, Phys. Rev. B **76**, 155313 (2007).
[14] W. Weber, Phys. Rev. Lett. **33**, 371 (1974).
[15] W. Weber, Phys. Rev. B **15**, 4789 (1977); K. C. Rustagi and W. Weber, Solid State Commun. **18**, 673 (1979); H. M. Tütüncü and G. P. Srivastava, Phys. Rev. B **53**, 15675 (1996); **62**, 5028 (2000).
[16] G. P. Srivastava and K. Kunc, J. Phys. C: Solid State Phys. **21**, 5087 (1988).
[17] H. M. Tütüncü, S. Bağci, and G. P. Srivastava, Phys. Rev. B **70**, 195401 (2004).
[18] S. P. Hepplestone and G. P. Srivastava, Phys. Rev. Lett. **101**, 105502 (2008); J. Appl. Phys. **107**, 043503 (2010).
[19] P. Keating, Phys. Rev. **145**, 637 (1965).
[20] W. J. Brya, Solid State Commun. **12**, 253 (1973).
[21] N. D. Lanzillotti-Kimura, A. Fainstein, A. Lemaitre, and B. Jusserand, Appl. Phys. Lett. **88**, 083113 (2006).
[22] B. Jusserand, D. Paquet, and A. Regreny, Phys. Rev. B **30**, 6245 (1984).
[23] A. K. Sood, J. Menéndez, M. Cardona, and K. Ploog, Phys. Rev. Lett. **54**, 2111 (1985).
[24] S. M. Lee, D. G. Cahill, and R. Vekatasubramanian, Appl. Phys. Lett. **70**, 2957 (1997).

[25] A. T. Khan, P. R. Berger, F. J. Guarin, and S. S. Iyer, Appl. Phys. Lett. **68**, 3105 (1996).
[26] H. A. Calderón, M. A. Vidal, and H. Ladrón de Guevara, Microsc. Microanal. **12**, 712 (2006).
[27] J. M. Ziman, *Electrons and Phonons* (Clarendon, Oxford, 1960).
[28] G. P. Srivastava, *The Physics of Phonons* (Adam Hilger, Bristol, 1990).
[29] W. Fon, K. C. Schwab, J. M. Worlock, and M. L. Roukes, Phys. Rev. B **66**, 045302 (2002); D. T. Morelli, J. P. Heremans, and G. A. Slack, *ibid.* **66**, 195304 (2002); W. Liu and A. Balandin, J. Appl. Phys. **97**, 073710 (2005), and references therein.
[30] P. Carruthas, Rev. Mod. Phys. **32**, 92 (1961).
[31] S. Y. Ren and J. D. Dow, Phys. Rev. B **25**, 3750 (1982).
[32] H. J. Monkhorst and J. D. Pack, Phys. Rev. B **13**, 5189 (1976).
[33] Y.-W. Mo, D. E. Savage, B. S. Swartzentruber, and M. G. Lagally, Phys. Rev. Lett. **65**, 1020 (1990); T. Ma, H. Tu, B. Shao, A. Liu, and G. Hu, Mater. Sci. Semicond. Process. **9**, 49 (2006).
[34] W. S. Capinski, H. J. Maris, T. Ruf, M. Cardona, K. Ploog, and D. S. Katzer, Phys. Rev. B **59**, 8105 (1999).
[35] A. Adams, IEEE. J. Select. Topics Quant. Electron. **PP**, 1 (1993).